Eur. Phys. J. Appl. Phys. **31**, 195–209 (2005)
DOI: 10.1051/epjap:2005059

THE EUROPEAN PHYSICAL JOURNAL
APPLIED PHYSICS

Wall shear stress in a laminar flow through a collapsed tube with wall contact

S. Naili[1,a], M. Thiriet[2,b], and C. Ribreau[1,c]

[1] Laboratoire de Mécanique Physique, CNRS UMR 7052 B2OA, Faculté des Sciences et Technologie, Université Paris XII–Val-de-Marne, 61 avenue du Général de Gaulle, 94010 Créteil Cedex, France
[2] Laboratoire Jacques-Louis Lions, CNRS UMR 7598, Université Pierre et Marie Curie, 75252 Paris Cedex 05, France, and Inria, action REO, BP 105, 78153 Le Chesnay Cedex, France

Received: 13 May 2004 / Received in final form: 25 March 2005 / Accepted: 17 May 2005
Published online: 14 September 2005 –

Abstract. The present work aims at studying mainly the wall shear stress of a laminar steady flow of an incompressible Newtonian fluid which is conveyed through a collapsed tube with a straight centreline. This tube is composed of a tapered segment, a contact segment where the opposite walls touch and a reopening segment. The tube geometry and steady flow characteristics are obtained from measurements in a collapsed tube. The Navier-Stokes equations associated with the classical boundary conditions are solved using the finite element method. The tridimensional flow results from the tube configuration. In particular, the flow consists of two side-jets due to two tear-drop shaped outer passages in the downstream contact segment associated with reversed flow. In order to compute both the stream-wise and cross-wise components of the shear stress on the wall, a local basis is defined in each wall node. Downstream of the contact segment, flow is separated in two jets which are studied though the help of the velocity field and the wall shear stress.

PACS. 47.15.-x Laminar flows – 47.60.+i Flows in ducts, channels, nozzles, and conduits – 83.50.Ax Steady shear flows, viscometric flow

1 Introduction

Flow through collapsible tubes has been widely investigated because it models certain biological flows, such as the blood flow in veins or the air flow in bronchi during forced expiration for example. Veins and bronchi can, indeed, collapse under sufficiently low transmural pressure (the difference between internal- and external pressure). Flows in collapsible tubes are also studied for industrial applications. For example, pharmaceutical industries use flexible channels for separation and purification processes. In biotechnologies, compliant tubes are used to control the flow rate for drug delivery; their collapsibility allows to achieve a very low flow rate over a week [1–3]. In hydrology, an auto-regulated device with constant discharge for irrigation networks was directly inspired by the compliant tube set-up [4]. A retention basin is equipped with a deformable pipe. The higher the water level of the basin is and, consequently, the higher the pressure to which the deformable pipe is subjected, the greater the pipe constriction is.

Over the past decades, many studies have analyzed the behavior of fluid flow through collapsible tubes. Measurements have been performed in a simple device, the Starling resistor [5]. A flow is conveyed through a thin-walled compliant straight tube which is mounted horizontally between two rigid tubes and enclosed in a rigid transparent chamber. The chamber pressure surrounding the compliant tube, the upstream and downstream pressures, the longitudinal tension and the volume flow rate can be adjusted. Results exhibit a set of peculiar phenomena. Among these, flow limitation which occurs when an increase in pressure drop fails to induce a flow-rate rise, due to either a choking mechanism or to viscous effects. Choking or "wave-speed limitation" is similar to flow limitation in gas flows through the throat of Laval nozzles or hydraulic jumps in shallow-water flows. To model these physical phenomena, theoretical works have to overcome a set of difficulties: (i) possible unstable behavior even with steady settings; (ii) possible time-dependant contact between the opposite tube walls; and (iii) the coupling between flow and tube's deformation. One-dimensional models, introduced by Oates [6], and revisited by Comolet [7] and Shapiro [8], although simple, were useful to understand flow phenomena such as flow limitation (e.g. [8] and [9] for a larger analysis). Two-dimensional models were proposed for a better understanding of wave propagation and oscillations in collapsible tubes (e.g. [9,10] and [11] for a review). Three-dimensional models were

[a] e-mail: naili@univ-paris12.fr
[b] e-mail: marc.thiriet@inria.fr
[c] e-mail: ribreau@univ-paris12.fr

initiated by Heil and Pedley [12]. However in these last models, the three-dimensional deformation of the wall was associated with a one-dimensional flow model. More recently, this model was improved to take into account three-dimensional flows at low Reynolds numbers without any wall contact [13]. At the opposite, the velocity field of a steady flow at high a Reynolds number in a strongly collapsed tube with wall contact was investigated for a frozen tube shape [14,15].

The collapsible-tube flow model exhibits a set of physical phenomena which were studied overlooking sometimes the connection with physiology. The main physical variables of interest are the pressure and velocity. However, collapsible-tube flow was also investigated to explain biological processes, at both macroscopic and microscopic scales. The metabolism of endothelial cells depends on the fluid stresses and their time and space gradients applied to the cells membrane. In particular, the wall shear stress was found to be a major factor affecting various functions of these cells. Most often, the biological functions of the endothelial cells are experimentally explored in flow chambers under controlled flow regime. In particular, straight collapsed channels with wall contact were designed to experiment the cell behavior when they were subjected to both traction and torque at the tube wall generated by a steady laminar fully developed flow [16]. The rigid channel has an axially uniform cross section. Other work was developed to investigate the steady laminar flow of incompressible fluid through a rigid smooth straight tube with axially-uniform collapsed cross sections [17,18]. The cross-section shape was found to affect the transverse distribution of the wall shear stress even after the entry length. The main conclusion from these studies is that the magnitude, the orientation and the space gradient – in steady conditions – of the wall shear stress must be known to determine the stimuli affecting the cell's functions.

Indeed, this earlier research showed that the endothelial cell response to flow varies and is highly sensitive to the spatial stresses. As far as the authors know, investigations of the wall shear stress has received little considerations in the literature for the non-uniformly collapsed tubes with a zone where the opposite walls are in contact. Although bi-lobed wall contact in veins remains questionable in everyday life, the vessel tapering and its flattening could to occur in vivo, at least in leg veins [19].

This article investigates the numerical simulation of a steady laminar flow of incompressible Newtonian fluid through a rigid collapsed tube. The shape of the collapsed tube has been reproduced from ultra-sound measurements of cross sections in a Starling resistor at a given flow conditions which have lead to a Reynolds number R_e equals 1210. Along of its axis, this tube exhibits three successive segments: (i) a tapered segment; (ii) a contact segment; and (iii) the reopening segment. Thus, the first aim of this study is to present the details of the three-dimensional velocity fields in this collapsed tube. A secondary aim is to design a numerical method in order to compute the viscous stress vector on the tube wall from the velocity field. This viscous stress vector is split in the normal and tangential components at the lateral surface of the tube. In order to explicit the contribution of the each component, a local basis is defined in each point of the lateral surface of the tube.

After this brief review, the method is introduced in Section 2, in particular the tube geometry definition, the numerical method used to solve the Navier-Stokes equations and to compute shear stresses at each point of the computational mesh. The results are described and discussed in Section 3.

2 Methods

2.1 Collapsed tube shape

A collapsible tube is attached on circular rigid tubes at both ends inside of a transparent box filled with water [14]. The downstream part of the tube is connected to a constant-level reservoir via a rigid tube. Water supply is ensured by gravity forces from a constant-head tank. Two in-parallel valves upstream from the test section ensures the volume flow-rate control. The volume flow-rate is measured by an electromagnetic flow-meter; the estimated relative error is approximately of 0.3%. Thin-walled elastic tubes, of elliptical unstressed cross-section (transmural pressure $p = 0$), have a density close to the water one. The frozen configuration used in the present study was defined for a flow rate of 16.2 ml.s^{-1}, i.e. for a Reynolds number R_e of 1210 calculated from the diameter and the cross-sectional average velocity in the inlet rigid tube.

The tube's axis $\mathbf{e}_z$ is related to the Cartesian framework $\mathbf{R}(O; \mathbf{e}_x, \mathbf{e}_y, \mathbf{e}_z)$, where O is the point situated on the z-axis at the inlet cross section and $(\mathbf{e}_x, \mathbf{e}_y, \mathbf{e}_z)$ an orthogonal basis for the space. An echograph is employed to visualize the shapes of selected tube's cross sections along the z-axis. The probe slides on a support aligned with the tube in order to limit measurement errors. The elastic tube was scanned especially in the segment of high cross-section variations. These cross sections are denoted by S_i, where i is an integer associated with the axial position. The two circular cross sections located at both ends are denoted by S_1 to S_{11}. The nine cross sections from S_2 to S_{10} are called the input cross sections in what follows and are respectively located at the axial positions from z_2 to z_{10}, given in Table 1. Following a convergent portion, between S_1 and S_8, the short contact portion, between S_8 and S_9, leads to a divergent, between S_9 and S_{11}.

The unstressed tube geometry (subscript 0) is measured, once fixed in the rigid box, before any flow experiment. The echographic images of the cross sections was digitalized by using Autocad software. The unstressed wall mid-line of the cross sections was fitted to an ellipse of area A_0 the perimeter of which was χ_0 [20]. Both A_0 and χ_0 were nearly constant along the tube length. The values of the major a_0 and minor b_0 semi-axes were calculated from $A_0 = \pi a_0 b_0$ and $\chi_0 \sim \pi((a_0^2 + b_0^2)/2)^{1/2}$; the closed-form solution of this system is given by $a_0 = 7.5$ mm and $b_0 = 6.3$ mm ($k_0 = a_0/b_0 = 1.2$). The thickness $h_0 = 0.3$ mm is given by the quadratic average of twenty

Table 1. The second line of the table gives the axial position z_i of the characteristic cross sections. The cross sections associated with the collapsed tube are denoted by S_i and their respective position is denoted by z_i for $i = 1, ..., 11$. The third line gives the cross sectional area of each characteristic cross sections.

input cross section	i_1	i_2	S_1	S_2	S_3	S_4	S_5	S_6
axial position (mm)	0.0	83.7	107.2	318.7	405.7	428.7	447.7	457.7
A (mm^2)	228.64	228.64	142.84	131.47	130.73	123.24	116.24	92.73

input cross section	S_7	S_8	S_9	S_{10}	S_{11}	o_1	o_2
axial position (mm)	463.7	471.7	478.7	485.7	490.2	520.6	604.3
A (mm^2)	72.46	37.74	23.84	100.98	142.84	228.64	228.64

measurements taken over the whole length of the collapsible tube.

The area of the digitized cross-sectional contours were identified to equivalent cross-section geometry, which were obtained from a computation using the model proposed by Ribreau et al. [21]. Briefly, the deformation model of an homogeneous infinitely long elastic tube of constant thickness submitted to an uniform negative transmural pressure on its lateral surface is based on the shell theory. The mechanical formulation corresponds to a two-dimensional problem in curvilinear medium and each cross section is described by a mid line, equidistant from the outer and inner boundaries of the cross section. The mid-line deformation of the elliptical cross-section wall is assumed to occur without length extension. Equivalent shapes of each cross section were defined by a set of 100 points located the wall mid-line in the positive quadrant ($x \geq 0$ and $y \geq 0$) of the Cartesian reference frame $\mathbf{R}$. The coordinates of the points which define the wetted perimeter are calculated from the coordinates of the corresponding mid-line points, knowing the angle at each point between $\mathbf{e}_x$ and the clockwise oriented unit tangent of the mid line and half the wall thickness. Luminal cross sections are displayed in Figure 1. In this figure, the upper and lower faces as well as the right and left edges have been defined in order to be used in what follows.

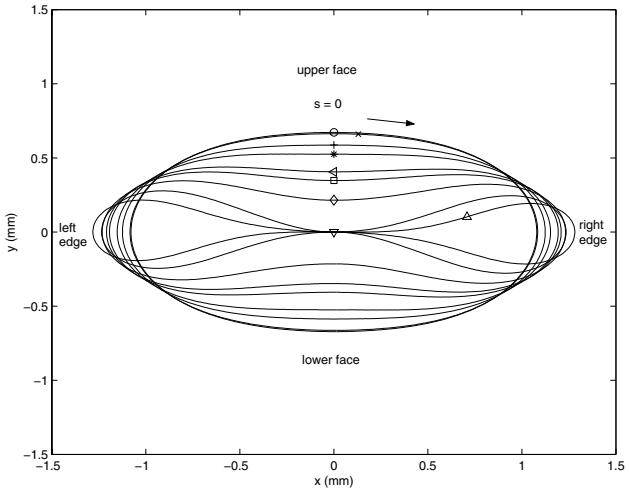

Fig. 1. The nine selected cross section shapes S_2 to S_{10} – marked by one single symbol – respectively located in z_2 to z_{10}. The wall mid-line used for the cross section and the wetted wall have been merged, i.e. the wall is assumed to have a zero thickness. The selected cross section stations are marked by: S_2 ($\circ\circ\circ$), S_3 ($\times\times\times$), S_4 ($+++$), S_5 ($***$), S_6 ($\square\square\square$), S_7 ($\diamond\diamond\diamond$), S_8 ($\triangledown\triangledown\triangledown$), S_9 ($\triangle\triangle\triangle$), S_{10} ($\triangleleft\triangleleft\triangleleft$). In addition, the origin of the arclength along the perimeter of the boundary cross section – $s = 0$ – and the clockwise direction to describe the wall shear stress along the perimeter are indicated. We have located the upper and lower faces as well as the right and left edges.

2.2 Computational domain: tube geometry

The whole tube (length of $L = 604.3$ mm) is decomposed into three main parts (Fig. 2): (i) a set of two uniform circular entrance pipe in series (length of 83.7 and 23.5 mm with a radius of 8.54 and 6.75 mm respectively), the second short pipe modeling the rigid attachment; (ii) the collapsed tube (length of 383 mm) which is described in the following paragraph; and (iii) a set of two uniform cylindrical pipes (length of 30.4 and 83.7 mm with a radius of 6.75 and 8.54 mm respectively), the first short pipe being the outlet attachment. The set of two circular uniform pipes in series at both inlet and outlet are called hereafter attachment ducts. The cross sections at both ends of the inlet attachment duct of the collapsed tube are denoted by i_1 and i_2, those which are located at the outlet are denoted by o_1 and o_2.

The collapsed tube is subdivided, in the stream-wise direction, into three successive segments: (i) a tapered segment (length of 364.5 mm) which starts with the inlet attachment duct; (ii) a contact segment (segment lying between the cross sections of the point-contact and the line-contact; this length is close to 7 mm, i.e. of 1.16% of the entire tube length or 1.83% of the collapsed tube length); and (iii) the reopening segment (length of 11.5 mm), which is attached to the outlet attachment duct. The contact segment is equivalent to a set of two symmetric outward channels; the edge x-coordinate increases because the central contact segment rises in length but the lumen decreases. The reopening segment diverges but not uniformly: the top and bottom walls diverge whereas its edges are convergent (see Fig. 3a, b).

Fourteen portions T_i define the whole tube and each portion T_i is bounded in the stream-wise direction z by two cross sections: (i) two in the set of entrance attachment ducts T_1 and T_2 (the first is situated between cross sections i_1 and i_2; and the second between i_2 and S_1); (ii) ten in the frozen collapsed tube from T_3 to T_9 (between S_1 and S_8) describing the tapered segment, T_{10} (between S_8

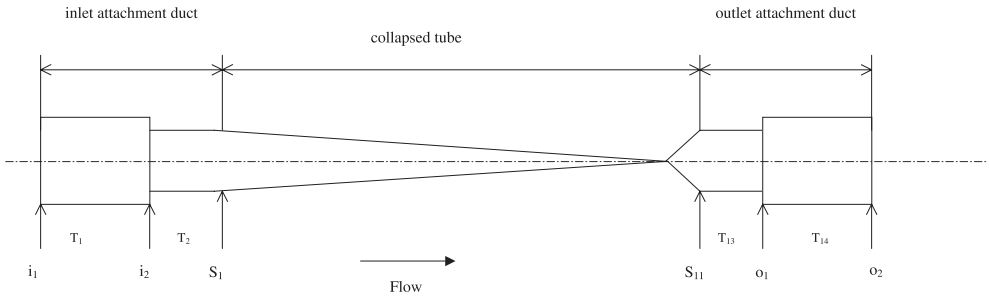

Fig. 2. Geometry of the collapsed tube with the measurement stations S_1 to S_{11}. The cross sections of the cylindrical duct, whose the cross section is circular, located at the inlet of the collapsed tube are denoted by i_1 and i_2. The cross sections of the cylindrical duct, whose the cross section is circular, located at the outlet of the collapsed tube are denoted by o_1 and o_2.

and S_9) being the contact segment, T_{11} (between S_9 and S_{10}) and T_{12} (between S_{10} and S_{11}) defining the reopening segment; and (iii) two in the set of exit attachment ducts T_{13} (between S_{11} and o_1) and T_{14} (between o_1 and o_2). In the divergent, the cross section S_{10} has a shape between those of S_5 and S_6.

In the sub-section which follows, the mathematical formulation of the flow modeling is presented as well as its numerical traitement which is based on a finite element method.

2.3 Flow modeling

The governing equations for the incompressible steady flow through the tube are given the Navier-Stokes equations which express the conservation of mass and momentum:

$$\nabla \cdot \mathbf{u} = 0; \quad (\mathbf{u} \cdot \boldsymbol{\nabla})\mathbf{u} = -\boldsymbol{\nabla} p_i + \nu \Delta \mathbf{u}, \tag{1}$$

where $\boldsymbol{\nabla}, \nabla\cdot$ and Δ symbols are respectively gradient, divergence and Laplace operators. Moreover, $\mathbf{u}$ is fluid velocity, p_i is the fluid pressure and ν is the fluid kinematic defined by the ratio μ/ρ, where μ and ρ are respectively the fluid dynamic viscosity and the fluid density.

In the formulation proposed in the present work, the pressure and body force are scaled by the fluid density. This formulation is commonly used in the field of computational fluid mechanics [22,23]. The advantage of this formulation lies in the fact that the same equation can have three interpretations: (i) if the kinematic viscosity is zero, the Navier-Stokes equations give Euler's equations for an incompressible fluid; (ii) if the kinematic viscosity is not zero, the classical Navier-Stokes equations are written with dimensional variables; (iii) if the velocity and the pressure fields represent non-dimensional variables, the kinematic viscosity is interpreted as the inverse of the Reynolds number. In the present work, the dimensional version of Navier-Stokes equations is preferred because the tube geometry came from image acquired in an experimental set-up. Furthermore, the conservation of momentum (1) gives the Stokes equation when the convective term is neglected. This last equation is used for computation initialization in the finite element method.

2.3.1 Boundary conditions

Let Γ_1 and Γ_2 be the inflow and outflow cross sections of the computational domain Ω respectively and Γ_3 the tube wall. The boundary conditions are:

$$\mathbf{u} = u_\Gamma \, \mathbf{e}_z \ \text{ on } \Gamma_1, \quad p_i = 0 \ \text{ on } \Gamma_2, \quad \mathbf{u} = \mathbf{0} \ \text{ on } \Gamma_3, \tag{2}$$

where u_Γ is the uniform injection velocity.

The first relation given by (2) imposes a flat velocity profile at the inlet and the last is the classical no slip condition on the lateral surface of the tube. The second relation (2) expresses an outflow condition applied to the boundary Γ_2.

2.3.2 Wall stress

At each point of the boundary Γ_3 of Ω, the viscous stress vector $\boldsymbol{\tau}$ associated with the viscous stress tensor $\mathbf{T}$, due to the scale, is defined by:

$$\boldsymbol{\tau} = \mathbf{T} \cdot \mathbf{n} = 2\nu \, \mathbf{D} \cdot \mathbf{n}, \tag{3}$$

where $\mathbf{n}$ is the inner unit normal vector of the boundary Γ_3 and $\mathbf{D}$ is the rate of strain tensor defined by:

$$\mathbf{D} = \frac{1}{2}(\boldsymbol{\nabla}\mathbf{u} + \boldsymbol{\nabla}\mathbf{u}^T), \tag{4}$$

where the superscript T denotes the transpose operator.

The stress vector $\boldsymbol{\tau}$ can be split into a normal and a tangential component respectively given by:

$$\boldsymbol{\tau}_n = (\boldsymbol{\tau} \cdot \mathbf{n})\mathbf{n}, \quad \boldsymbol{\tau}_s = (\mathbf{I} - \mathbf{n} \otimes \mathbf{n}) \cdot \boldsymbol{\tau} \tag{5}$$

where $\otimes$ means the tensor product.

The relation (3) can be expressed in the Cartesian basis $(\mathbf{e}_x, \mathbf{e}_y, \mathbf{e}_z)$ by:

$$\begin{aligned} \boldsymbol{\tau} = \nu \Big\{ & \Big[(2u_{x,x}n_x + (u_{x,y} + u_{y,x})n_y + (u_{x,z} + u_{z,x})n_z \Big] \mathbf{e}_x \\ & + \Big[(u_{x,y} + u_{y,x})n_x + 2u_{y,y}n_y + (u_{y,z} + u_{z,y})n_z \Big] \mathbf{e}_y \\ & + \Big[(u_{x,z} + u_{z,x})n_x + (u_{y,z} + u_{z,y})n_y + 2u_{z,z}n_z \Big] \mathbf{e}_z \Big\}. \end{aligned} \tag{6}$$

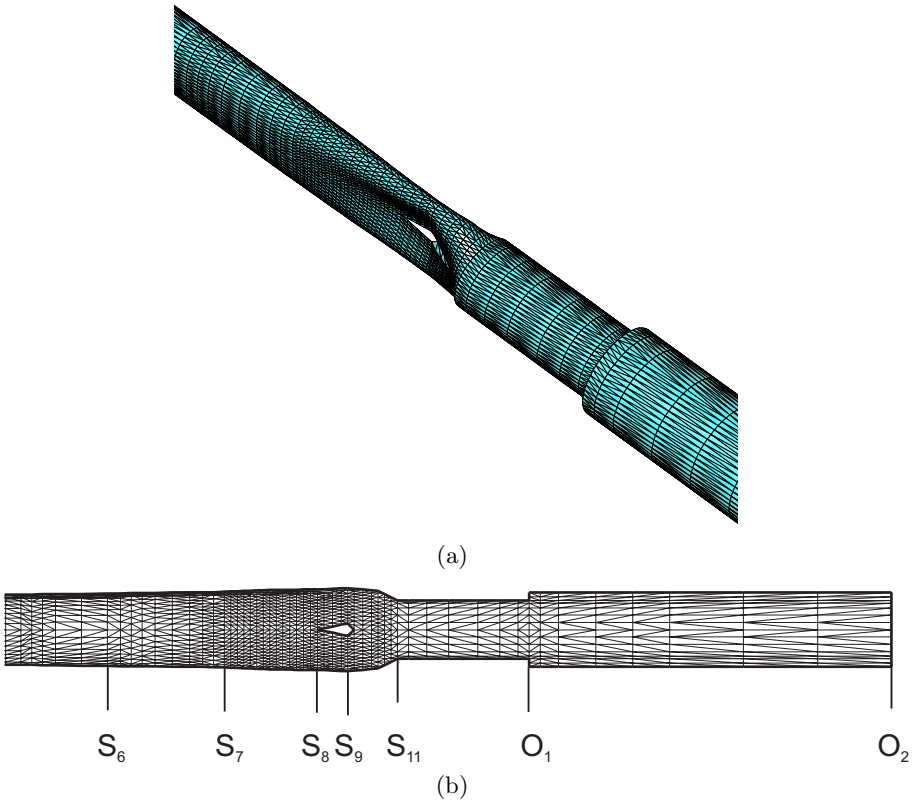

Fig. 3. (a) 3D surface mesh of distal segment of the collapsed tube and the outlet cylindrical duct in series. (b) Top view in the centerplane ($y = 0$) of the portion of interest in the contact segment and in the outlet attachment duct.

In the last relation, the x-component of $\mathbf{u}$ in the Cartesian basis $(\mathbf{e}_x, \mathbf{e}_y, \mathbf{e}_z)$ is denoted by u_x. The partial derivative of u_x with respect to y is designated by $u_{x,y}$. The same notation is used for every vector component and every partial derivative.

To obtain the decomposition into the sum of two vectors described by (5), the stress vector $\boldsymbol{\tau}$ is expressed in a local basis. On the surface Γ_3, let $\mathbf{t}$ the transverse tangent unit vector, which is perpendicular to $\mathbf{n}$ and belongs to the plane of the cross section. The vector $\mathbf{t}$ is tangent to the boundary of the cross section and is oriented in the anticlockwise direction. Let $\mathbf{b} = \mathbf{t} \wedge \mathbf{n}$, where $\wedge$ designates the cross product. The unit vector $\mathbf{b}$ is parallel to $\mathbf{e}_z$ in the straight segments of the test section but not in its collapsed part. The Frenet trihedron $(P; \mathbf{n}, \mathbf{t}, \mathbf{b})$ is then defined in each point P of Γ_3. The vector $\boldsymbol{\tau}$ is expressed in this trihedron with its components (τ_t, τ_n, τ_b) by the following formula:

$$\begin{aligned}\boldsymbol{\tau} &= \boldsymbol{\tau}_n + \boldsymbol{\tau}_s \\ &= J\,[(t_y b_z - t_z b_y)\tau_x + (t_z b_x - t_x b_z)\tau_y \\ &\quad +(t_x b_y - t_y b_x)\tau_z]\mathbf{n} + J\Big\{[(b_y n_z - b_z n_y)\tilde{\tau}_x \\ &\quad +(b_z n_5 34x - b_x n_z)\tau_y + (b_x n_y - b_y n_x)\tau_z]\mathbf{t} \\ &\quad +[(n_y t_z - n_z t_y)\tau_x + (n_z t_x - n_x t_z)\tau_y \\ &\quad +(n_x t_y - n_y t_x)\tau_z]\mathbf{b}\Big\}, \end{aligned} \tag{7}$$

where J is the determinant of the Jacobian matrix of the Cartesian-to-Frenet frame change:

$$J = b_x(n_y t_z - n_z t_y) - b_y(n_x t_z - n_z t_x) + b_z(n_x t_y - n_y t_x). \tag{8}$$

2.4 Numerical method

2.4.1 Mesh generation

The tube geometry is symmetric with respect to the meridian plane normal to the centerplane (i.e. $x = 0$) and to the centerplane (i.e. $y = 0$). Thus, a mesh for the quarter of the configuration is first generated. This mesh is defined for $z \geq 0$ and in the positive quadrant of the plane defined by $x \geq 0$ and $y \geq 0$. For each portion T_i $(i = 1, 2, \ldots, 14)$, the five surfaces of interest are: quarters of two successive cross sections (S_i, S_{i+1}), the lateral surface defined between these quarters of cross sections and the two surfaces corresponding to the intersection of the tube geometry and the symmetry planes.

Only a quarter for each input cross section S_i, the one in the positive quadrant, is meshed. Each mesh is obtained from the coordinates of the points of the wall contour but also segments on axes $x = 0$ and $y = 0$. The cross section wall is defined from the minimum number of 15 points fitting the wall contour. The 15 point distribution is not uniform along the arclength between two consecutive cross

sections S_i because wall curvature changes from one cross section to the other; their cross coordinates (x, y) vary thus from one cross section to the next one. In addition, the mesh is refined with a thick layer at the lateral surface to avoid a discontinuity in the velocity field at the domain entry. Uniform injection velocity at the inlet still results in high entry wall shear stress.

Once the fourteen surfaces are meshed for each quarter of the geometry, they are assembled to give the piece of interest. Then the intersection surfaces are merged to give the test section surface of the geometry quarter. Finally, the three-dimensional domain is meshed using the TetMesh-GHS3D software (INRIA research project GAMMA [24], sold by Simulog [25]). It creates automatically and quickly a tetrahedral volume mesh out of a closed triangular surface mesh, under the condition that the surface meshed has neither no surface holes nor intersections. The whole mesh is carried out by two successive symmetries with respect to $x = 0$ and $y = 0$ planes to avoid numerical artifacts due to mesh asymmetry. A part of this mesh, focused on the contact segment and the reopening segment, is displayed in Figure 3a. Moreover, the top view in the centerplane ($y = 0$) of the segments of interest is shown in Figure 3b. The numbers of vertices and of tetrahedra are equal to 15.538 and 76.484 respectively.

2.5 Numerical solution of the Navier-Stokes equations

2.5.1 Weak formulation

The numerical solution of the Navier-Stokes equations is based on a variational formulation of the governing equations which is defined by:

find $\mathbf{u} \in \mathbf{V}$ and $p_i \in Q$ such that:

$$\begin{cases} a(\mathbf{u},\mathbf{v}) + c(\mathbf{u};\mathbf{u},\mathbf{v}) + b(\mathbf{v},p_i) = 0, & \forall\, \mathbf{v} \in \mathbf{V}_0 \\ b(\mathbf{u},q) = 0, & \forall\, q \in Q \end{cases} \tag{9}$$

where the bilinear forms a: $\mathbf{V}\times\mathbf{V} \longrightarrow \mathbb{R}$ and b: $\mathbf{V}\times Q \longrightarrow \mathbb{R}$ are defined by:

$$a(\mathbf{u},\mathbf{v}) = \nu \int_\Omega \mathrm{Tr}\left((\boldsymbol{\nabla}\,\mathbf{u})^T \boldsymbol{\nabla}\,\mathbf{v}\right)\, dv,\ \forall\, \mathbf{u},\mathbf{v} \in \mathbf{H}^1(\Omega) \tag{10}$$

and

$$b(\mathbf{v},q) = -\int_\Omega q\, \boldsymbol{\nabla}\cdot\mathbf{v}\ dv,\ \forall\, \mathbf{v} \in \mathbf{H}^1(\Omega), \forall\, q \in L^2(\Omega) \tag{11}$$

where Tr designates the trace operator, dv is the differential element of the volume and $\mathbb{R}$ the set of real numbers.

The trilinear form c: $\mathbf{V}\times\mathbf{V}\times\mathbf{V} \longrightarrow \mathbb{R}$ is defined by:

$$c(\mathbf{w};\mathbf{u},\mathbf{v}) = \int_\Omega \mathbf{w}\cdot\boldsymbol{\nabla}\mathbf{u}\cdot\mathbf{v}\ dv,\ \forall\, \mathbf{u},\mathbf{v},\mathbf{w} \in \mathbf{H}^1(\Omega). \tag{12}$$

Throughout, $\mathbf{H}^1(\Omega)$ and $L^2(\Omega)$ denote respectively the Sobolev space of order 1 defined on Ω for vector-valued functions and the space of functions that are square integrable in the Lebesgue sense with respect to Ω.

In this variational formulation, all terms make sense if the following test function spaces are chosen:

$$\mathbf{V}_0 = \left\{\mathbf{v} \in \mathbf{H}^1(\Omega) \mid \mathbf{v} = \mathbf{0} \ \text{ on } \ \Gamma_1 \ \text{ and } \ \Gamma_3\right\}, \tag{13}$$

$$\mathbf{V} = \left\{\mathbf{u}\in\mathbf{H}^1(\Omega) \mid \mathbf{u} = u_\Gamma\, \mathbf{e}_z \text{ on } \Gamma_1 \text{ and } \mathbf{u} = \mathbf{0} \text{ on } \Gamma_3\right\}, \tag{14}$$

$$Q = L^2(\Omega). \tag{15}$$

2.5.2 The discrete problem

The spatial discretization is based on finite elements defined with the aid of the P_1 bubble/P_1 element where velocities and pressure are respectively approached [26]. On each tetrahedra element, the pressure p_i is defined at the four vertices of the tetrahedron (P_1 element) and the velocity $\mathbf{u}$ at both the vertices and the barycentre (P_1 bubble element). Even in the case of a steady flow, the computational method is based on the search of the solution of the equations describing an unsteady flow. In this case, the time plays the role of a parameter which allows the iterations until convergence — steady flow. The time discretization uses a fractional step scheme of order 2 which is described by Boukir et al. [27]. The convection step is processed by a characteristic method [28]. The computation is initialized as a Stokes problem. The solution is obtained via a generalized Uzawa-preconditioned-conjugate gradient method [22]. The order of the method is $\mathcal{O}(\xi^2)$ for $\mathbf{u}$ and $\mathcal{O}(\xi)$ for p_i in the $L^2(\Omega)$ norm where the parameter ξ is the characteristic size of the tetrahedron.

The solution convergence towards a steady flow is based on the $L^2(\Omega)$ norm of the residuals of the flow quantities which is quickly divided by, at least, a factor of 10^{-5} and remains nearly constant. Convergence is usually obtained after a time lower than the duration to cover a characteristic line [28], used to compute the non-linear convection term, with the suitable time step. The distance travels by the characteristic line is usually equal to four times the tube length.

2.5.3 Computation of the wall viscous stress vector

The wall stress vector is computed once the velocity field is known, especially at the nodes of boundary tetrahedra. In addition, only the information obtained at the vertex of each element are used to simplify the computations. Thus, owing to the type of finite element used, the velocity field is class $C^2(\Omega)$ ($C^2(\Omega)$ designates the space of all two time continuously differentiable functions). Using relation (4), we have calculated the rate of strain tensor from the 3D velocity field and the viscous stress tensor $\mathbf{T}$. To this end, we have used an interpolation by Lagrange polynomials of degree one. Accordingly, the viscous stress tensor obtained on each tetrahedron is constant and can differ substantially when calculated in adjacent elements if a coarse finite element is used. When the finite element mesh is refined, the differences between adjacent elements decrease but the spatial variations of the stress tensor remain discontinuous at the facets between two adjacent

elements. Once the unit normal vector on all the facets of the lateral surface Γ_3 determined, the viscous stress vector is computed from the viscous stress tensor accordingly to relation (6). Since the viscous stress tensor is constant, the viscous stress vector is also constant on each facet of Γ_3. The local basis defined by the Frenet trihedron associated with each facet of Γ_3 is determined from the unit normal vector of the corresponding facet. The viscous stress vector obtained previously is then projected in the local Frenet trihedron by using the relations (7) and (8). From this vector which is calculated on each facet of Γ_3, the viscous stress vector at each node of Γ_3 is computed using a weighting procedure. For a given node on Γ_3, a weighted average of the whole set of the contributions of the neighboring facets is computed using the area of the facet as the weighting factor.

3 Results and discussion

The arclength along the quarter of the wall of cross section is convenient to display the results. The arclength origin from which the contour is covered in the clockwise direction, is located at mid-face of the upper wall, i.e. at the intersection point between the wall and the y-axis (Fig. 1). The opposite wall is defined as the lower face. The junctions of both faces define the right and left edges, i.e. intersection of the wall and x-axis.

3.1 Velocity

The velocity field is displayed using the velocity variation along the centerline, the velocity profiles along the symmetry axes in the input cross sections and the vector plots of the projected velocities in the cross-section planes. The results are presented in order to detail the three-dimensional structure of the flow, with lateral jets and flow separations in the pinched and reopening segments of the tube.

3.1.1 Centerline velocity

The variations of the axial velocity component u_z along the tube centerline from the S_7 is given in Figure 4. The centerline velocity reaches its maximum upstream from and near S_8. In S_8, the opposite walls (here defined as the upper and lower faces) are in contact at a single point located on the centerline. This point, which corresponds to the vertex of the leading edge of the contact segment, is impacted by the flow. Moreover, S_8 has the smallest cross-sectional area of the tapered segment (Tab. 1). Its area has been indeed divided by about four from its value at the tapered tube entry. Upstream from S_8, the centerline velocity rises. But the centerline velocity value do not give the highest velocity at a given axial station. The maximum velocity is indeed displaced towards the tube edges in the downstream segment of the tapered part due the formation of the two sideways streams. Downstream from S_8 (between S_8 and S_9), the mid-faces are in contact.

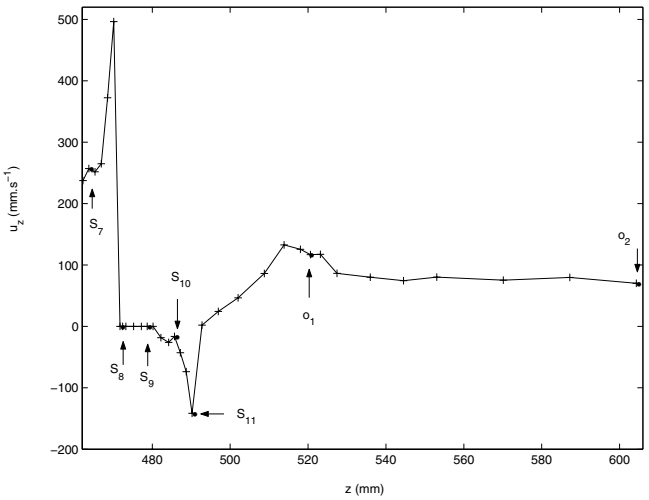

Fig. 4. Variations of axial velocity component u_z along the centerline of the test section from S_7 cross section station. On the curve, the position of cross sections has been marked by a bullet point (•).

Consequently, the fluid flows outside the tube axis, along the wetted sides of the contact segment. The negative centerline velocity in the reopening segment is explained by flow separation behind S_9, as observed at a trailing edge of an immersed body. In the upstream part of the reopening segment, the fluid conveyed at high speed from each lateral channel separated by the contact walls moves toward the tube axis. Downstream from S_{11}, the centerline velocity increases to a maximum which is located slightly upstream from o_1 between the two tubes of the exit attachment duct. Downstream from o_1, the centerline velocity decreases slightly to reach an almost constant value throughout most of the length between o_1 and o_2. The centerline velocity in this segment is nearly equal to its entrance value.

3.1.2 Velocity profiles in the $y = 0$ plane

Figure 5 gives the u_z profile in the centerplane (plane $y = 0$) in the cross-section set S_1 to S_{11} and o_2. For the sake of clarity, the figure has been split in two parts: (i) Figure 5a for the stations in the tapered segment S_1 to S_7; (ii) Figure 5b for stations in the contact and reopening segments S_8 to o_2. In the tapered segment, the decrease in cross-sectional area is first associated with a flattening of the upper and lower faces and then with a curvature inversion at mid-faces. Whereas the y-coordinate of the mid-faces decreases in the stream-wise direction from S_1 to S_7, the x-coordinate of the tube edge increases. The change in cross sectional shape is greater in the downstream segment of the tapered tube part than the upstream contact segment. In Figure 5a, the velocity profiles are plotted over the x-axis; the length of which increases when the cross section is located farther and farther from the tube entry because the edges becomes farther and farther to the centerline. At the opposite, in the reopening segment from S_9

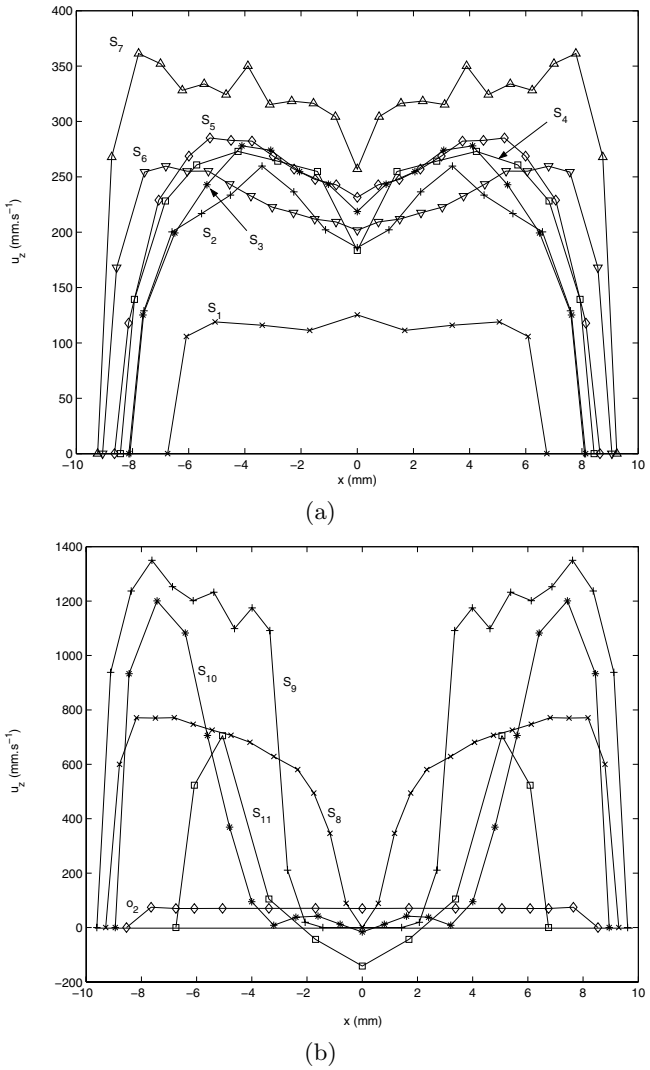

Fig. 5. (a) Variations of axial velocity component u_z along the x-axis at the selected cross section stations: S_1 ($\times\times\times$), S_2 ($+++$), S_3 ($***$), S_4 ($\square\square\square$), S_5 ($\diamond\diamond\diamond$), S_6 ($\triangledown\triangledown\triangledown$), S_7 ($\triangle\triangle\triangle$). This region of the collapsed tube characterizes convergent part. (b) Variations of axial velocity component u_z along the x-axis at the selected cross section stations: S_8 ($\times\times\times$), S_9 ($+++$), S_{10} ($***$), S_{11} ($\square\square\square$), o_2 ($\diamond\diamond\diamond$). This region of collapsed tube characterizes successively the contact segment, divergent tube part and exit straight duct.

to S_{11}, the upper and lower faces are divergent whereas the edges are convergent. In the reopening segment, the length of the x-axis decreases when the cross sections is located closer and closer from the tube exit, because the edges becomes closer and closer to the centerline. In Figure 5b, the velocity profiles are plotted over the x-axis; the length of which decreases when the cross sections is located farther and farther from the tube entry because the mid-faces becomes closer and closer to the centerline.

Since the velocity profile is flat at the inlet cross section i_1 (uniform injection velocity), a boundary layer develops in the stream-wise direction but the velocity profile in S_1 exhibits a very slightly developed flow. Between S_1 to S_2, the velocity has been multiplied by a factor of about 2 while the cross-sectional area decreases (8% in relative difference). Station S_2 (211.5 mm downstream from S_1 and 153 mm upstream from S_8) is defined by nearly flat mid-face regions. The velocity profile in S_2 is characterized by two lateral velocity maxima. These maxima are located about half-way between the tube axis and the edges. The relative difference between the centerline velocity and the velocity maximum is equal to about 30%. The position in the cross section of the velocity maxima remains in the centerplane and migrates towards the edges as the cross section is closer to the contact zone. It becomes close to the edge wall in S_7. Whatever the axial position, the velocity gradient near the wall is large.

In the contact segment from S_8 to S_9, each peak velocity is close to the tube edge. Whereas the cross-sectional area decreases with a factor of about 37% between S_8 and S_9, the maximum velocity is multiplied by a factor of about 1.8 (relative difference of 53%) over this short distance. Downstream from S_9, the maximum velocity gradually goes centerwards. In the reopening segment, the velocity profiles are dromedary-back shaped. In S_{11}, its value is slightly lower than the peak value in S_8 (relative difference of 9%). In S_8 and S_9, the velocity decreases highly in the inward direction and strongly near the wall contact as well as near the edges. In contrast, the velocity decreases abruptly from its maximum and reaches negative values in the core region of S_{10} and S_{11}. Reversed flow in the core region of the centerplane of the reopening segment is exhibited by negative axial velocities. The minimum velocities in S_{10} and S_{11} are located on the centerline. The relative difference between the velocity minimum and maximum are equal to about 1% in S_{10} and 20% in S_{11}. Whatever the axial position, the velocity gradient near the wall remains large. In S_{11}, located 11.5 mm downstream from S_9, the flow remains greatly disturbed. Further downstream, the fluid continues to flow inwards in the exit pipe.

3.1.3 Velocity profiles in the $x = 0$ plane

Figure 6 shows u_z profiles in the $x = 0$ plane. In S_1, the velocity profiles in the $x = 0$ and $y = 0$ planes are quantitatively similar in Figure 5a and in Figure 6a. Further downstream in the tapered segment, velocity maxima are located in or close by the centerline. The velocity profiles are plotted over the y-axis; the length of which decreases when the cross sections is located farther and farther from the tube entry because the mid-faces becomes closer and closer to the centerline. The maximum velocity increases by a factor of about 2 between S_1 and S_7. Whatever the axial position, the velocity gradient near the wall is large. In contrast with the velocity profiles along the x-axis (Fig. 5a), the velocities are negative or null along the y-axis in the contact and reopening segments (Fig. 6b). Because S_9 is characterized by a contact line between its opposite walls, no fluid flows along the y-axis and its neighboring region (no curve for this input station

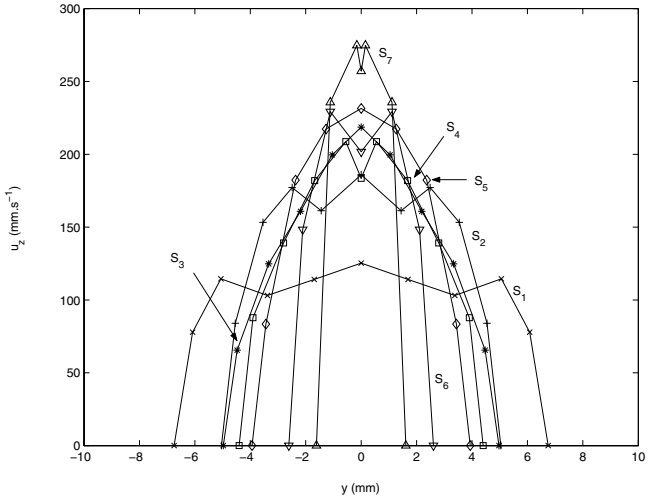

(a)

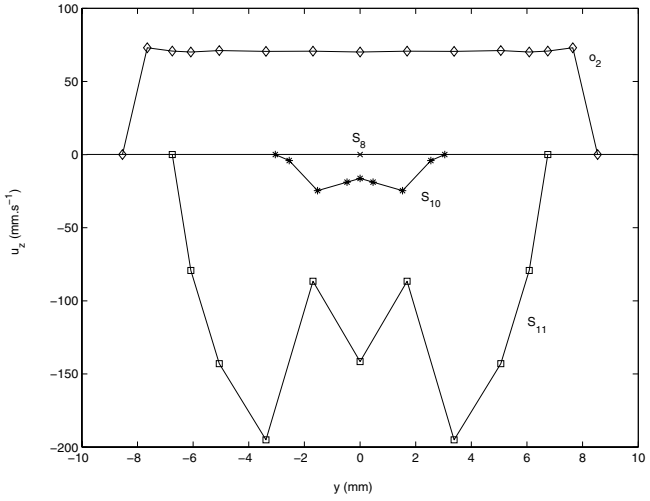

(b)

Fig. 6. (a) Variations of velocity component u_z along the y-axis at the selected cross section stations: S_1 ($\times\times\times$), S_2 ($+++$), S_3 ($***$), S_4 ($\square\square\square$), S_5 ($\diamond\diamond\diamond$), S_6 ($\triangledown\triangledown\triangledown$), S_7 ($\triangle\triangle\triangle$). (b) Variations of velocity component u_z along the y-axis at the selected cross section stations: S_8 ($\times\times\times$), S_9 ($+++$), S_{10} ($***$), S_{11} ($\square\square\square$), o_2 ($\diamond\diamond\diamond$).

in Fig. 6b). In the outlet attachment duct, slightly upstream from o_1, the axial velocity is positive throughout the $x = 0$ plane.

3.1.4 Velocity cross displays

Thiriet and Ribreau [15] has shown that the maximum velocity was located outwards in the centerplane, in agreement with the velocity profiles plotted in the centerplane in the present work. Downstream from the lobes of the contact segment, two inwards jets occur in the reopening segment characterized by converging edges and diverging mid-faces. The jets, defined by high fluid velocities, persist throughout the upstream half of the outlet attachment duct. Because the wall mid-face regions are divergent, the jet momentum diffuses across the tube lumen, especially upwards and downwards. In the outlet attachment duct (circular cross section), four high velocity regions, with a magnitude close to the highest velocity observed in S_7, appear near the y-axis at a height of about the half radius. Consequently, abrupt changes in the velocity distribution occur in the exit pipe.

Velocity components in the planes of the cross sections are displayed from S_4 to S_{11} in Figure 7. Cross currents, here defined as the streams displayed by the velocity components (u_x, u_y) in the plane of the cross section, provide an useful tool to describe and to analyze the three-dimensional nature of the flow. In the upstream part of the tapered segment, the velocity vector plots show four swirls located in the four quadrants of the cross section with respect to two symmetry axis. These swirls are symmetrical with respect to both the x and y axes. The motion in the positive quadrant ($x \geq 0$ and $y \geq 0$) is anticlockwise (e.g. Fig. 7a). Downstream from S_5 down to S_8, the wall converging upper and lower mid-faces play the role of sources with cross currents towards the core region and along the wall. Sinks are located at the edges as shown from Figure 7b–d. In the contact segment, the source-sink type of secondary motion is also observed as displayed in Figure 7e, f. Here, the source is located at the contact point between opposite walls. In the reopening segment, high cross currents near the edges are the images of the jets exiting from the lobes, with an inwards and up(down)wards direction. Moreover, a set of four swirls, which are centered in the core region, appears. Downstream from S_{10} additional swirls are located near the mid-face to form twin eddies in each quadrant of the cross section (Fig. 7g, h). This is more obvious from Figure 8a, b which display the fluid trajectories in the cross sections. At the exit of the outlet attachment duct, the cross currents become negligible due to the selected exit boundary conditions.

3.2 Wall shear stress

The variations of axial τ_b and cross τ_t components of the wall shear stress (in Pa) are plotted in the input cross sections S_i along the quarter of the arclength s (iso-z, τ vs. s curves) or along lines of given s (iso-s, τ vs. z curves). The cross component is defined by the vector component in the plane of the cross section. In the case of the shear stress, the component of interest τ_t is tangential to the wall.

3.2.1 Axial component τ_b of the wall shear stress

Spatial changes in wall shear stress along the wetted perimeter χ at the selected cross sections are illustrated in Figure 9. For the sake of clarity, the figure has been split in two parts: (i) Figure 9a for the stations in the tapered segment S_1 to S_7; (ii) Figure 9b for stations in the contact segment. The perimeter $\chi = \chi_0$ is constant for the set of

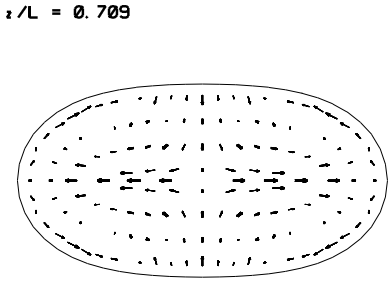

(a)

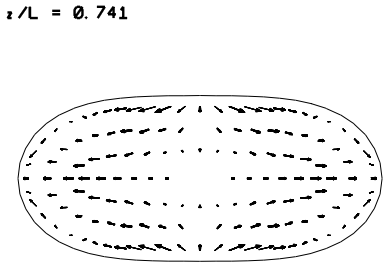

(b)

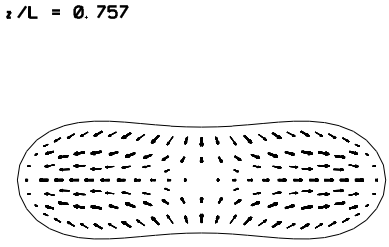

(c)

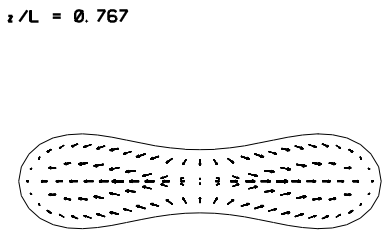

(d)

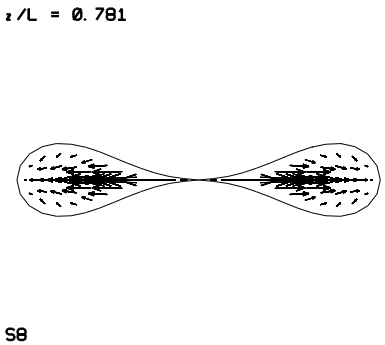

(e)

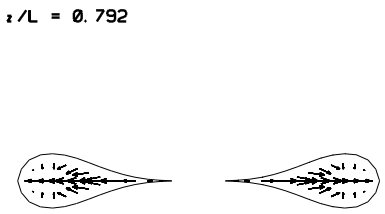

(f)

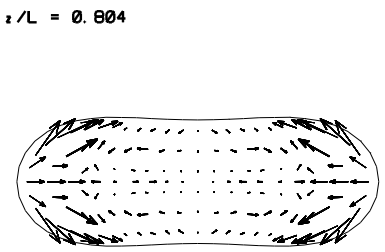

(g)

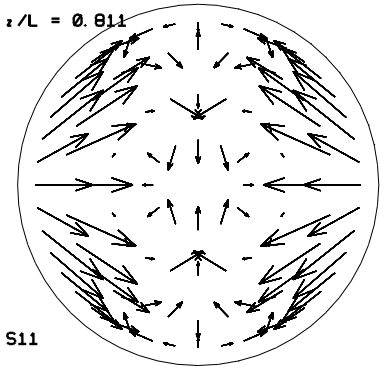

(h)

Fig. 7. (a) Cross components (u_x, u_y) at the selected cross section station S_4. The dimensionless axial position z/L is given in the figure (length of $L = 604.3$ mm). The scale used to drawn the magnitude of the field velocity is 0.07. (b) Same caption as in (a) but at the selected cross section station S_5. The scale used to drawn the magnitude of the field velocity is 0.07. (c) Same caption as in (a) but at the selected cross section station S_6. The scale used to drawn the magnitude of the field velocity is 0.02. (d) Same caption as in (a) but at the selected cross section station S_7. The scale used to drawn the magnitude of the field velocity is 0.01. (e) Same caption as in (a) but at the selected cross section station S_8. The scale used to drawn the magnitude of the field velocity is 0.01. (f) Same caption as in (a) but at the selected cross section station S_9. The scale used to drawn the magnitude of the field velocity is 0.01. (g) Same caption as in (a) but at the selected cross section station S_{10}. The scale used to drawn the field velocity of the arrow is 0.01. (h) Same caption as in (a) but at the selected cross section station S_{11}. The scale used to drawn the magnitude of the field velocity is 0.01.

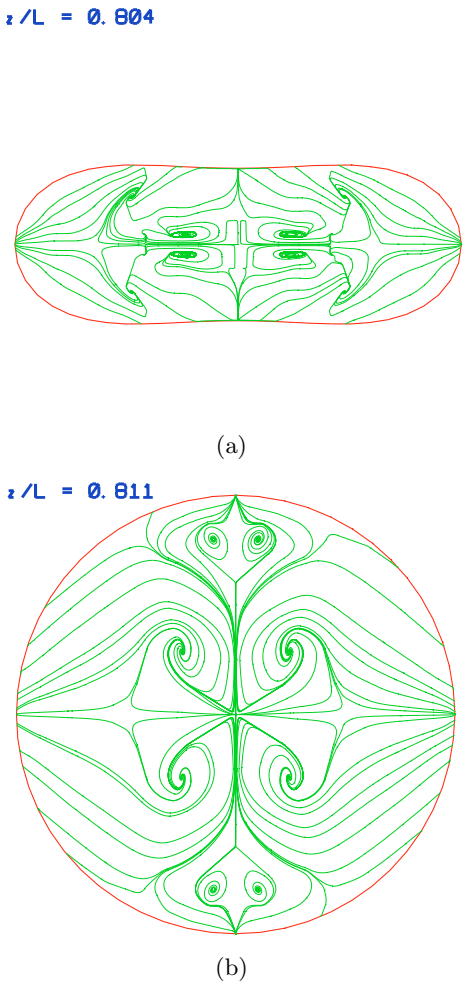

Fig. 8. (a) The traces of fluid trajectories in the cross section S_{10}. (b) The traces of fluid trajectories in the cross section S_{11}.

selected axial stations because these collapsed configurations correspond to transmural pressure $p > p_\ell$, where p_ℓ is the line-contact pressure [9]. In the cross sections of the tapered segment, τ_b decreases from its mid-face ($s = 0$) value with increasing s down to a minimum and then rises to its edge value ($s = \chi_0/4$). The variations of the wall shear stress (Fig. 9a) are higher and higher when the cross section is located farther and farther from the tube entry. In the contact segment, τ_b increases from $s = 0$ up to its maximum which is closer to the mid-face in S_8 than in S_9 (Fig. 9b). It decreases then down to a minimum and then rises up to its edge value. In the reopening segment, τ_b increases from $s = 0$ to $s = \chi_0/4$ (Fig. 9c). Its value is negative over about the inner third of $\chi_0/4$.

Spatial variations in τ_b have also been plotted along two lines defined by $s = 0$ and $s = \chi_0/4$ shown in Figure 10a, b respectively. These two circumferential positions correspond to the common nodes of the discretized wall whatever the cross section. In the collapsed tube, τ_b is positive at the edge but it becomes null or negative at mid-face between S_{10} and S_{11} due to flow reversal (Figs. 5a and 6b). At the opposite, τ_b becomes negative

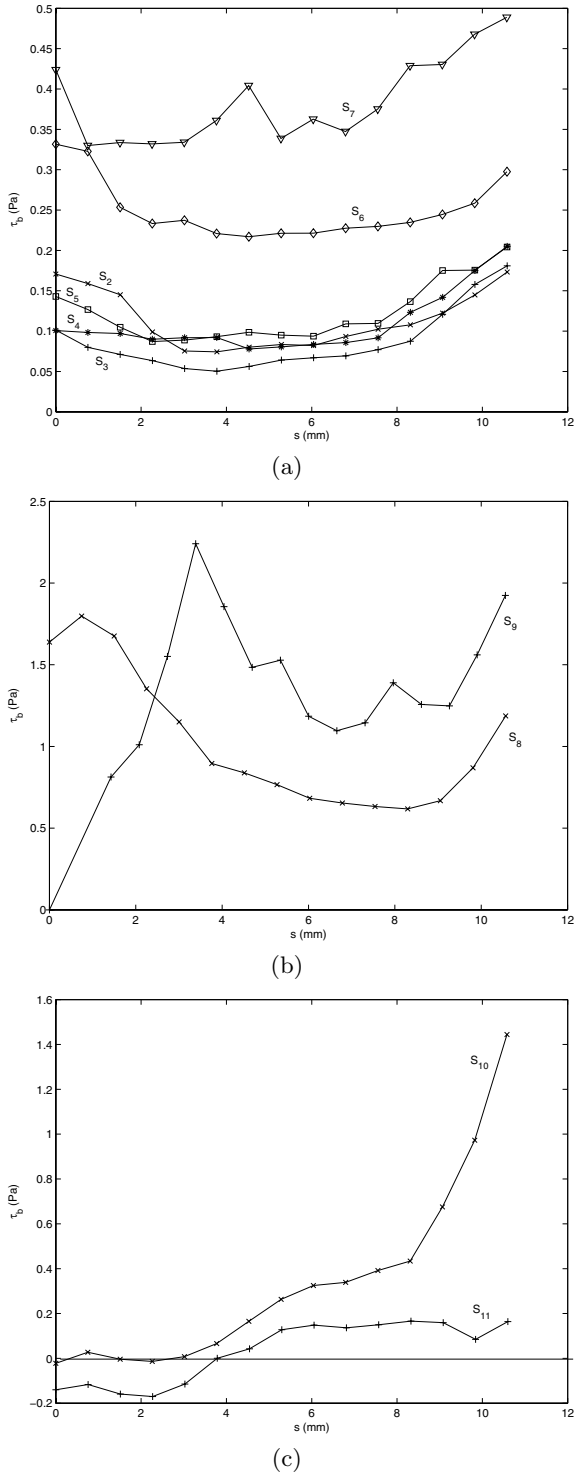

Fig. 9. (a) Variations of shear stress component τ_b along the arclength s at the selected stations: S_2 ($\times\times\times$), S_3 ($+++$), S_4 ($***$), S_5 ($\square\square\square$), S_6 ($\diamond\diamond\diamond$), S_7 ($\triangledown\triangledown\triangledown$). This region of the collapsed tube characterizes convergent part. (b) Variations of shear stress component τ_b along the arclength s at the selected stations: S_8 ($\times\times\times$), S_9 ($+++$). This region of the collapsed tube characterizes strongly collapsed part. (c) Variations of shear stress component τ_b along the arclength s at the selected cross section stations: S_{10} ($\times\times\times$), S_{11} ($+++$). This region of the collapsed tube characterizes the divergent part.

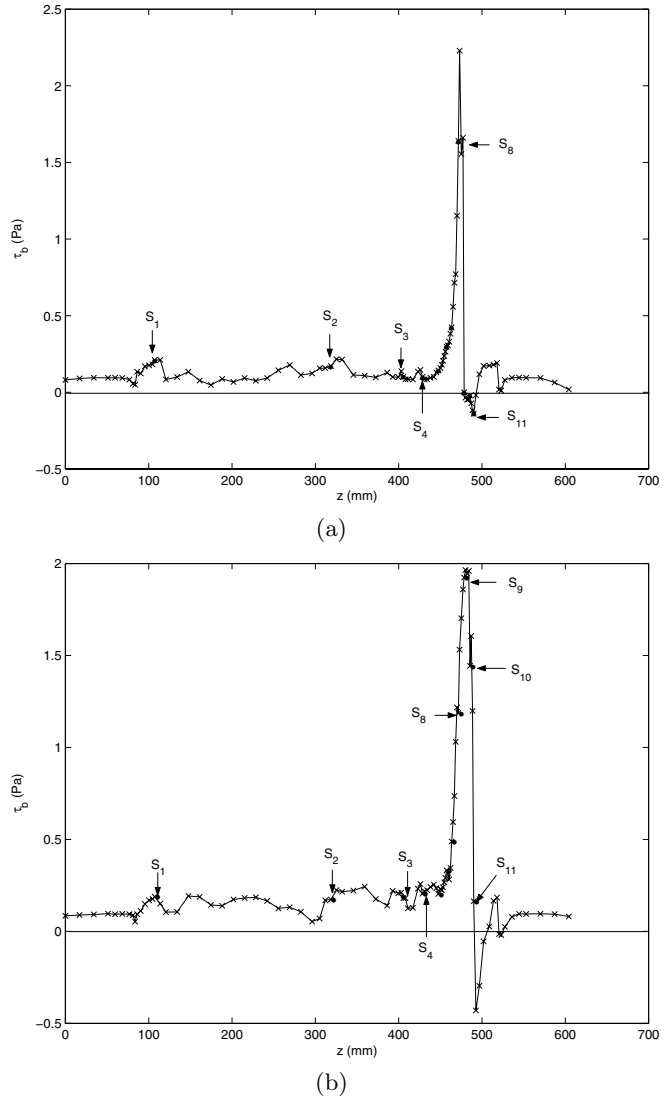

Fig. 10. (a) Variations of shear stress component τ_b along the tube length at the mid-face ($x = 0$ plane). On the curve, the position of cross sections has been marked by a bullet point (•). (b) Variations of shear stress component τ_b along the tube length at edge ($y = 0$ plane). On the curve, the position of cross sections has been marked by a bullet point (•).

at the edge in the entrance segment of the outlet attachment duct due to another flow reversal while the lateral jet is going towards the centreline. The axial component τ_b remains almost constant between S_1 and S_5 at both the mid-face and the edge. The component τ_b rises abruptly from S_5 to its maximum in the contact segment for both selected values of s and decreases rapidly in the reopening segment. In both the inlet and outlet attachment ducts, τ_b reaches similar values.

3.2.2 Cross component τ_t of the wall shear stress

Spatial changes in cross component τ_t of the wall shear stress along χ_0 at the selected axial stations are illustrated in Figure 11. In the upstream part of the tapered segment, i.e. from S_2 to S_4, τ_t remains nearly constant because the flow in this region is not highly disturbed by the downstream wall contact (Fig. 11a). At the opposite, in the downstream part of the tapered segment, i.e. from S_5 to S_7, τ_t decreases from $s = 0$ with increasing s down to a minimum and then rises to its edge value ($s = \chi_0/4$). Due to the direction of the cross current from the mid-face to the edge (Fig. 7d), τ_t is negative. In S_8 (contact segment), τ_t decreases quickly to a minimum which is equal to about two third of the local value of τ_b. The sudden decrease in τ_t near the wall contact is explained by the strong outwards motion of the fluid streams which enters in the lobes, as demonstrated by the cross currents (Fig. 7e). It rises then gradually to its zero value at the edge. In S_9, spatial changes in τ_t along s exhibits three extrema: a first maximum near the wall contact, then a minimum at a cross site close to the location of the first maximum, and a second maximum near the edge (Fig. 11b). The values of τ_t in S_9 are much lower than in S_8; but its minimum is twice the minimum in S_7. In the reopened part, τ_t is negative over about one third of $\chi_0/4$. Along this perimeter part, τ_t decreases to a minimum which have the same magnitude than the local value of τ_b. With increasing s, τ_t rises up to its maximum near the edge, which is about twice the minimum in absolute value, to decrease then to zero at the edge. In S_{10}, the maximum value of τ_t is about half the local value of τ_b while in S_{11} it is about 1.5 times the local value of τ_b (Fig. 11c). At the mid-face and at the edge for every selected station, τ_t is equal to zero due to the sink-source motion type of the cross currents.

3.3 Validation

The Navier-Stokes solver has been tested using various benchmarks with internal and external flows. Different common kinds of immersed bodies (cylinders, spheres) were investigated before carrying out numerical tests around cars, train wheels, planes and boats (see e.g. [22]). Usual benchmarks were also explored for pipe flows, like backward steps. Comparison between numerical and experimental results of time-dependent flows in a 90 degree bend (curvature ratio of 1/10) shows a good agreement (in particular, the maximum velocity moves from the outer edge to the inner bend during the flow cycle [29]).

Checking was carried out in four complementary directions. (i) Numerical simulations were performed on straight collapsed tubes of axially uniform cross section at different Reynolds number using two Navier-Stokes solvers based on different finite element type [18]. The maximum relative difference between the two velocity fields is lower than 9%, using the same meshes for each investigated cases. The mean relative difference is equal to about 4%. (ii) Flow quantities computed downstream from the entry length in the straight tubes of uniform circular cross section at different Reynolds number were compared to the Poiseuille solution. The numerical solutions of the fluid velocity and the wall shear stress are respectively calculated with a maximal relative error of 3% and 4% for

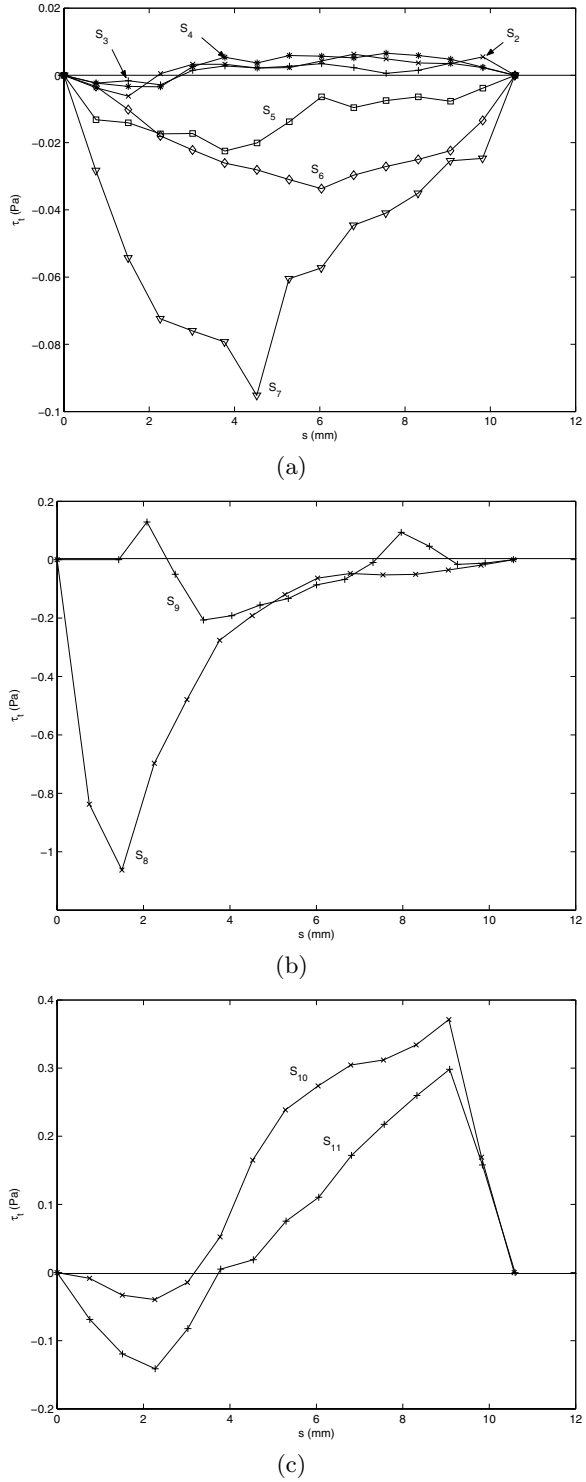

Fig. 11. (a) Variations of shear stress component τ_t along the arclength s at the selected stations: S_2 ($\times\times\times$), S_3 ($+++$), S_4 ($***$), S_5 ($\square\square\square$), S_6 ($\diamond\diamond\diamond$), S_7 ($\triangledown\triangledown\triangledown$). This region of the collapsed tube characterizes convergent part. (b) Variations of shear stress component τ_t along the arclength s at the selected stations: S_8 ($\times\times\times$), S_9 ($+++$). This region of the collapsed tube characterizes strongly collapsed part. (c) Variations of shear stress component τ_t along the arclength s at the selected cross section stations: S_{10} ($\times\times\times$), S_{11} ($+++$). This region of the collapsed tube characterizes divergent part.

three Reynolds numbers (35, 500 and 1000) [17,18]. (iii) The fully-developed velocity profiles obtained in the three-dimensional in uniformly collapsed tubes were compared to the two-dimensional results, given in [21] but using the same cross-section meshes. A maximal relative error of 4% was found on the whole set of collapsed configurations. (iv) The mesh of the surface of the reopening segment was refined in order to evaluate the mesh sensitivity. The mesh element number has been locally increased by a factor of 44%. Although the velocity fields were not wholly superimposed, the results did not exhibit any significant qualitative and quantitative differences.

3.4 Relevance of the present work

In flow chambers, the shear stress was shown to affect the endothelial cell functions not only by its local magnitude but also by its space and time gradients. The present work deals with steady flow; consequently, only spatial gradients are considered. Previous investigations were carried out in rigid straight pipes characterized by an uniform cross section whose shape mimics uniformly collapsed tubes. Such configurations might be observed in inclined deformable vessels when viscous effects balance hydrostatic forces [9]. The cross shape with its change in wall cross curvature induces transverse gradients in wall shear stresses. Because the flow in the present experiment is not fully developed, there is also an axial gradient in wall shear stresses. Such studies were useful to provide the entry length and the wall shear stress field in experimental cell-coated pipes with the same cross configuration. In the present work, the duct has the axial shape defined by the axial transmural pressure gradient set in a stationary condition such that wall contact occurs near its outlet, over a small but significant length. This axial configuration, obtained by a three-dimensional reconstruction from a Starling resistor does not wholly mimic physiological state. However, the tapered segment models ascending superficial collapsed veins (more compliant than the deep veins) of the inferior limbs in some circumstances. Iso-z, τ_b vs. s curves are relatively different from those obtained in uniformly collapsed tubes with similar cross configurations in most cross sections. Only in S_9, the axial wall shear stress have spatial variations similar to those in uniformly collapsed tubes with contact configuration.

The location of τ_b maximum along the wetted wall of the cross section depends on the distance between the opposite wall faces and the variations in wall curvature. A linear relation between the wall shear stress and the wall cross curvature may be found in Poiseuille flow because in this case the cross section is circular and the curvature of its boundary is constant. However, when the cross curvature varies strongly, the relationships between the wall shear stresses and the wall curvature of the cross section are non-linear. Moreover, a drastic reduction in the cross sectional area is associated with an increase in the axial wall shear stress for a fixed Reynolds number. Between S_1 and S_9, the cross sectional area is divided by 6 whereas

the shear stress maximum is multiplied by 13. Vein collapse might thus induce larger loading on the endothelial cells with respect to dilated veins.

3.5 Literature data

The presentation of the literature works is focused on 3D experimental and numerical investigation in steady collapsed tube. Laser-Doppler velocimetry has been performed in a rigid tube with a local bi-lobed stenosis without contact of the opposite walls associated with a transverse enlargement [30]. Such an very localized configuration do not model accurately a collapsed configuration. Nevertheless, this tube configuration imposes two lateral jets on edges as those already observed in a two-dimensional domain [31]. Hazel and Heil [13] computed a steady collapsed tube configuration without contact of the opposite walls. Once the tube configuration is obtained, these authors explored the flow, prescribing a Poiseuille flow at the tube inlet and stress-free condition at the outlet. Poiseuille flow is an usual boundary condition when the steady laminar flow is assumed to be fully developed at the entry of the test section. It is associated with much smaller wall shear stress than with uniform injection velocity. In the present work, the collapsed tube is located downstream an inlet attachment duct in which flow is developing. Hazel and Heil used the finite element method with hexahedron associated with Q_1 element (tri-linear basis function) for the pressure and Q_2 element (tri-quadratic basis function) for the velocity. The steady laminar flow was studied for the three values of the Reynolds number 64, 191 and 350, which is based on the unstressed tube radius and the cross-sectional average velocity. Whatever the Reynolds number, the minimum cross-sectional area remains the same. The external pressure is thus adjusted. Their collapsed tube is shorter than our deformed pipe. In the most collapsed segment of the test section, high velocity streams are found near the edges. As in the present work, the velocity increases a lot in this segment (Fig. 4 of [13]). Two symmetrical high velocity streams appear upstream and inside the exit attachment duct. The momentum transport in this segment of the test section is associated with vortices centered near the tube axis displayed by the cross streamlines, especially at $Re = 350$ (Fig. 9 of [13]). Such flow features are similar to our results. In absence of any wall contact, the fluid is flowing in the core region throughout the whole collapsed tube length.

4 Conclusion

The flow of a Newtonian incompressible fluid, governed by the Navier-Stokes equations, is conveyed through a collapsed tube with a zone where the opposite walls are in contact. The tube shape mimics a configuration obtained from ultra-sound measurements in a Starling resistor. The flow behavior is affected by both the tube shape and by the flow conditions (a Reynolds number larger than 1000 associated with a maximum velocity of about 1.4 $\mathrm{m.s}^{-1}$).

The present computational model provides the spatial changes in the velocity and the wall shear stress. The tube configuration yields a three-dimensional flow with important gradient of the flow quantities in both the streamwise and cross-wise directions. The three-dimensional flow structure in steady conditions is defined by a set of swirls in the divergent downstream from the contact segment in the core behind the wall contact and along the diverging walls. Two side jets emerging from the contact segment of the collapsed tube run towards and outward the two tube centerplanes respectively; they partially merge in the upstream segment of the exit attachment duct.

References

1. A. Abdul Nour, R. Cannon, M.Y. Jaffrin, Innov. Tech. Biol. Med. **10**, 133 (1989)
2. B. Dion, S. Naili, J.P. Renaudeaux, C. Ribreau, Med. Biol. Eng. Comput. **33**, 196 (1995)
3. B. Dion, S. Naili, J.P. Renaudeaux, C. Ribreau, Med. Biol. Eng. Comput. **33**, 838 (1995)
4. D. Vischer, P. Peter, La Houille Blanche **2**, 123 (1985)
5. F.P. Knowlton, E.H. Starling, J. Physiol. **44**, 206 (1912)
6. G.C. Oates, Med. Biol. Eng. **13**, 773 (1975)
7. R. Comolet, C. R. Acad. Sci. Paris, Série B **283**, 41 (1976)
8. A.H. Shapiro, J. Biomech. Eng.-T. ASME **99**, 126 (1977)
9. M. Thiriet, S. Naili, A. Langlet, C. Ribreau, Modelling of thin walled tubes with a flowing fluid and their applications in the study of the collapse of anatomic vessels, edited by C. Leondes, *Biomechanical Systems: Techniques and Applications, volume IV of Biofluid Methods in Vascular and Pulmonary Systems* (CRC Press, 2001), Chap. 10, pp. 1–43
10. T.J. Pedley, J. Biomech. Eng.-T. ASME **114**, 60 (1992)
11. M. Heil, O.E. Jensen, Flows in deformable tubes and channels – theoretical models and biological applications, edited by T.J. Pedley, P.W. Carpenter, *Flow in Collapsible Tubes and Past Other Highly Compliant Boundaries*, (Kluwer, Dordrecht, Netherlands, 2003), Chap. 2, pp. 15–50.
12. M. Heil, T.J. Pedley, J. Fluid. Struct. **9**, 237 (1995)
13. A.L. Hazel, M. Heil, J. Fluid Mech. **486**, 79 (2003)
14. M. Benmbarek, *Écoulement laminaire permanent dans un modèle de veine*, Ph.D. thesis, Université Paris XII, 1997
15. M. Thiriet, C. Ribreau, Mec. Ind. **1**, 349 (2000)
16. C. Haond, C. Ribreau, O. Boutherin-Falson, M. Finet, Eur. Phys. J. Appl. Phys. **8**, 87 (1999)
17. S. Naili, M. Thiriet, C. Ribreau, Eur. Phys. J. Appl. Phys. **17**, 139 (2002)
18. M. Thiriet, S. Naili, C. Ribreau, Comput. Modeling Eng. Sci. **3**, **4**, 473 (2003)
19. S. Bassez, P. Flaud, M. Chauveau, J. Biomech. Eng.-T. ASME **123**, 58 (2001)
20. C.D. Bertram, C. Ribreau, Med. Biol. Eng. Comput. **27**, 357 (1989)
21. C. Ribreau, S. Naili, M. Bonis, A. Langlet. J. Biomech. Eng.-T. ASME **115**, 4(A), 432 (1993)
22. O. Pironneau, *The finite element methods for fluids* (John Wiley & Sons, 1989)

23. M.D. Gunzburger, Navier-stokes equations for incompressible flows: finite element methods. edited by R. Peyret, *Handbook of computational fluid mechanics* (Academic Press, 1996), Chap. 3, pp. 99–157
24. Project GAMMA. Automatic mesh generation and adaptation methods, inria (france), 2003. Web page `http://www.inria.fr/recherche/equipes/gamma.en.html`
25. TetMesh-GHS3D, Simulog (France), 1993
26. R. Glowinski, *Numerical methods for nonlinear variational problems* (Springer-Verlag, New York, 1984)
27. K. Boukir, Y. Maday, B. Metivet, A high order characteristics method for incompressible navier-stokes equations. in *Proceedings of International Conference on Spectral and High Order Method, Montpellier (France), June, 1992*
28. O. Pironneau, Numer. Math. **38**, 309 (1982)
29. M. Thiriet, *Étude des écoulements dans les voies respiratoires intrathoraciques proximales et les artères de gros calibre de la circulation systémique*, Ph.D. thesis, Habilitation à Diriger des Recherches, Université Denis Diderot, 1994
30. C.D. Bertram, S.A. Godbole, J. Biomech. Eng.-T. ASME **119**, 357 (1997)
31. C. Ribreau, S. Naili, A. Langlet, J. Fluid. Struct. **8**, 183 (1994)